Analysis of fault-induced electromechanical disturbance effect in a closed-loop system

Urszula Jachymczyk[1], Pawel Knap[1], and Krzysztof Lalik[1]

[1] *AGH University of Krakow, Kraków, 30-059, Poland*
ujachymczyk@agh.edu.pl
pknap@agh.edu.pl
klalik@agh.edu.pl

ABSTRACT

This paper examines whether motor current can provide a useful proxy for bearing faults in a closed-loop drive system. In such systems, the controller continuously adjusts current to maintain the operating point, which can hide small fault-related increases in losses and make overall current consumption a weak health indicator. To address this problem, current signatures from the Paderborn University bearing dataset were analyzed using 23 indicators covering global current level, band-limited residual ripple, envelope-based features, and classical sideband measures. These indicators were ranked according to class separability, stability in healthy measurements, and robustness to residual operating-condition variation. Their physical relevance was further explored by predicting selected current indicators from vibration features. The analysis shows that better discrimination is obtained when the analysis is shifted from total current level to residual ripple content, where fault-induced effects are significant enough to be visible and distinguishable from noise. Among the tested features, the band 105-2000 Hz features consistently provided the best separation between healthy and faulty bearings across 4 operating conditions. These results suggest that, for closed-loop drives, band-limited current features are promising monitoring inputs for sensor-light diagnostics.

1. INTRODUCTION

Vibrations are considered one of the most sensitive and effective indicators for early fault detection in rotating machinery (Randall, 2011). They are directly related to fault conditions and losses caused by induced friction, which lead to increased power consumption and reduced efficiency (Brkovic et al., 2017). The occurrence of faults results in an increase in vibration energy (Son, 1982) and a decrease in drive efficiency (Bishop, 2024). For example, in a water pumping station, bearing faults increased vibration levels by up to 85%, while power consumption rose by 14% and efficiency dropped by 18% (Abu-Zeid & Abdel-Rahman, 2013). Power consumption, maintenance, and initial investment costs account for 85%, 10%, and 5% of the total life-cycle cost of a pumping station, respectively (Ackerman, 2023). By introducing drive misalignment in the range of 0–20%, electrical efficiency deteriorated significantly and the power factor decreased from 0.9 to 0.4 (Korolev, 2025). For induction motors, bearing damage reduced efficiency by three percentage points under constant mechanical output corresponds to roughly a 4% increase in input power (Garcia, Panagiotou, Antonino-Daviu, & Gyftakis, 2019).

1.1. Power losses vs operating conditions

In electromechanical drive systems, electrical power consumption is determined not only by the technical condition of the machine but also by the operating point, including load torque, rotational speed, control mode, supply quality, and temperature. Even under nominally healthy operation, changes in torque demand, supply quality, or thermal state may produce variations that are larger than the incremental losses introduced by an early fault (Sousa Santos, Cabello Eras, Sagastume Gutierrez, & Cabello Ulloa, 2019).

Therefore, the objective is not simply to observe whether current or power consumption increases but to identify which part of that change is attributable to fault-induced dissipation rather than to normal shifts of operating conditions. This motivates the search for indicators that are less dependent on the global current magnitude and more sensitive to fault-related ripple, modulation, or band-limited energy redistribution (Yang, Pen, Wang, & Chang, 2016; Chen et al., 2023).

1.2. Power losses in closed-loop control systems

The interpretation of electrical power and current becomes even more challenging in closed-loop drive systems. In

inverter-driven machines operating with speed or torque control, the stator current is an actively manipulated control variable (Gritli et al., 2017). A developing fault may increase local dissipation or ripple generation, while the controller simultaneously acts to preserve the commanded speed or torque, thereby masking the fault in global quantities such as RMS current or average input power. Faults in bearings and other mechanical components often manifest instead as additional modulation, sidebands, or broadband residual energy around the dominant electromechanical components (Yang et al., 2016; Bravo-Imaz et al., 2017), making ripple-oriented features more suitable.

This difficulty is compounded by the fact that, in inverter-fed motors, the diagnostic content of the stator current depends not only on the fault itself but also on the converter topology (Martin-Diaz et al., 2017). Bearing fault detection achieved 97% accuracy for line-fed motors but only 71% for inverter-fed motors (Kilickaya & Eren, 2025). Consequently, motor-current-based fault detection in closed-loop systems must remain robust under changing operating conditions, transient regimes, and control-induced spectral distortion, often requiring feature selection (Jachymczyk, Knap, & Lalik, 2025), adaptive or order-tracking techniques (Liu & Bazzi, 2017; Gritli et al., 2017).

2. RESEARCH GAP & CONTRIBUTION

Existing studies suggest that bearing faults can increase losses and reduce drive efficiency, but this evidence comes mainly from induction-motor or application-specific studies. In closed-loop systems however, the measured motor current reflects not only machine condition but also control action, operating-point variation, and measurement noise.

Consequently, the unresolved issue is not simply whether bearing faults leave traces in motor current, but whether those traces can be isolated in a simple and physically interpretable way in closed-loop, inverter-fed operation. Although recent studies show that bearing-fault information can be extracted from built-in electrical signals, they also indicate that the diagnostic content is strongly band-dependent and influenced by the control structure (Santer, Reinhard, Schindler, & Graichen, 2025). Current feature-extraction and classification methods lack systematic determination of
(i) which residual-current frequency bands carry fault-sensitive yet operating-point-robust information,
(ii) how these bands relate to characteristic bearing-fault frequencies and their harmonics,
(iii) or whether they provide separability comparable to classical fault-frequency-based indicators.
Thus, a clear gap remains in establishing whether band-limited residual-current RMS indicators can reveal mechanically meaningful fault effects in closed-loop drives and how their separability compares with classical fault-frequency-based indicators.

2.1. Research Scope

The present study evaluates band-limited RMS indicators over several candidate frequency ranges, with the aim of identifying bands in which fault-induced ripple is sufficiently visible while remaining less sensitive to operating-point variability and closed-loop control noise. The effectiveness of indicators is compared across multiple operating conditions and fault severities.

The study is designed to answer the following research questions:

- **RQ1:** Can increased motor current consumption be associated with bearing faults in a closed-loop drive system and constant operating conditions?
- **RQ2:** Which frequency bands in the motor current signal contain the strongest fault-induced fluctuations compared to disturbances caused by closed-loop control and operating conditions?
- **RQ3:** To what extent do indicators derived from these current frequency bands provide separability comparable to or better than classical bearing fault indicators?
- **RQ4:** Can these current fluctuations in selected frequency bands be explained by vibration features, indicating that they originate from mechanical fault dynamics?

3. PADERBORN UNIVERSITY (PU) DATASET

The experiments in this study were conducted using the Paderborn University (PU) bearing dataset (Lessmeier, Kimotho, Zimmer, & Sextro, 2016). The PU test rig is a modular electromechanical drivetrain composed of a permanent-magnet synchronous motor (PMSM) with $p = 4$ pole pairs, a torque-measuring shaft, a rolling-bearing test module, a flywheel, and a load motor. The measured signals include motor phase currents and housing vibration signals in high-rate frequency (64 kHz), while mechanical signals, rotational speed, load torque, and radial force are recorded in 4 kHz. Additionally, the temperature value was measured with 1 Hz.

The experiments were performed with 32 different bearing states in total: 6 healthy bearings, 12 bearings with artificially induced damage, and 14 bearings with real damage. The severity of damages varies from 1 to 3. Considered bearing defects are:

- outer ring,
- inner ring,
- multiple or combined damage patterns.

According to the bearing documentation, the relevant geometrical parameters of the 6203 bearing are $N_B = 8$, $D_P = 28.55$ mm, $D_B = 6.75$ mm, and $\theta = 0°$.

The official benchmark contains four operating conditions defined by combinations of rotational speed, load torque, and radial force: `N15_M07_F10`, `N09_M07_F10`, `N15_M01_F10`, and `N15_M07_F04`. For each bearing state and operating condition, 20 recordings of 4 s duration were acquired.

4. METHODOLOGY

The research problem considered in this work is whether bearing faults in a closed-loop inverter-fed drive can be detected from motor current despite the fact that the measured current is simultaneously influenced by controller action, inverter-related distortion, and small operating-point variations. Under these conditions, fault effects are expected to appear not mainly as a clear increase in total current magnitude, but rather as weak changes in residual ripple and modulation content. Therefore, the methodology is designed to identify current band indicators that are sensitive to such fault-related ripple, compare their diagnostic usefulness, and then verify whether the most informative indicators are physically related to mechanical fault dynamics through vibration-based prediction.

4.1. Indicator Definitions

For each window, the phase currents were first mean-centered and then converted to a two-phase space vector:

$$i_\alpha = i_1, \qquad i_\beta = \frac{i_1 + 2i_2}{\sqrt{3}}, \tag{1}$$

$$i_{\mathrm{sv}} = \sqrt{i_\alpha^2 + i_\beta^2}. \tag{2}$$

Because the dominant electrical component can mask weaker fault-related modulations, a narrow zero-phase IIR notch filter centered at f_S with a $\pm 2\ Hz$ sideband width was applied. All ripple-oriented band indicators were computed from $i_{\mathrm{sv,notched}}$, whereas the raw RMS and sideband indicators were using i_{sv}.

4.1.1. Indicators Set

The feature set contained the following 23 indicators in total:

- 2 primary global RMS indicators,
- 8 primary normalized band-ripple indicators,
- 2 secondary global envelope-RMS indicators,
- 8 secondary envelope-band indicators,
- 3 FFT-based sideband indicators.

Where direct RMS and band-ripple indicators serve for capturing the overall current ripple, while envelope- and sideband-based quantities were interpreted only as reference indicators, which may allow for better separability across fault classes but are no directly tied to increased current ripple caused by faults.

Primary amplitude and ripple indicators Pure RMS is intended to capture the overall current level and the remaining ripple after suppression of the dominant electrical component.

$$y_{\mathrm{RMS}} = \mathrm{RMS}(i_{\mathrm{sv}}), \tag{3}$$

$$y_{\mathrm{RMS,clean}} = \mathrm{RMS}(i_{\mathrm{sv,notched}}). \tag{4}$$

To localize this ripple in frequency, candidate band-pass filtered signals were defined as the normalized band RMS:

$$y_{[f_\ell, f_h]} = 100 \cdot \frac{\mathrm{RMS}(\mathrm{BP}(i_{\mathrm{sv,notched}}, f_l, f_h))}{\mathrm{RMS}(i_{\mathrm{sv,notched}}) + \varepsilon}, \qquad \varepsilon = 10^{-8}. \tag{5}$$

where BP denotes band-pass filtering over the interval $[f_l, f_h]$.

This normalization was used to express the band-limited ripple energy relative to the residual cleaned current level. In this way, the indicator emphasizes how strongly a given frequency band contributes to the post-notch current signal.

The analyzed candidate bands are listed in Table 1.

Table 1. Candidate frequency bands considered for ripple-sensitive current indicators.

Band	Frequency range [Hz]
A	20–150
B	20–300
C	70–180
D	1000–2000
E	105–2000
F	20–2000
G	75–1000
H	105–32000

The candidate bands were selected considering the range in which bearing-fault-related current components may occur, while also testing both lower- and higher-frequency residual ripple regions:

- A: low-frequency residual ripple, including lower-order sidebands,
- B: extended low-frequency ripple, including the full set of first-order sidebands,
- C: frequency region in the neighborhood of the fundamental component,
- D: high-frequency ripple content, dominated by harmonic modulation,
- E: post-fundamental broadband residual, including higher-order sidebands,
- F: wideband ripple summary,
- G: intermediate-band residual ripple,

- H: post-fundamental high-passed band.

Secondary envelope-based comparison indicators Envelope-based indicators were also computed in order to examine whether classical demodulation-style descriptors provide clearer fault separation than the direct ripple-energy measures defined above.

The global envelope RMS quantities were defined as

$$y_{\mathrm{RMS,env}} = \mathrm{RMS}(|\mathcal{H}\{i_{\mathrm{sv}}\}|)\,, \tag{6}$$

$$y_{\mathrm{RMS,clean,env}} = \mathrm{RMS}(|\mathcal{H}\{i_{\mathrm{sv,notched}}\}|)\,, \tag{7}$$

where $\mathcal{H}\{\cdot\}$ denotes the Hilbert transform.

For each candidate band, an envelope-based counterpart was defined as

$$y^{\mathrm{env}}_{[f_\ell,f_h]} = \mathrm{RMS}\big(\big|\mathcal{H}\left\{x_{[f_\ell,f_h]}\right\}\big|\big)\,. \tag{8}$$

FFT-based sideband indicators. The sideband indicators were subsequently calculated from the frequency domain by applying a Hann window $\tilde{i}_{\mathrm{sv}}[n]$ and computing the corresponding one-sided FFT magnitude spectrum:

$$X[k] = \mathrm{FFT}\left\{\tilde{i}_{\mathrm{sv}}[n]\,w[n]\right\}, \qquad f_k = \frac{kf_s}{N}, \tag{9}$$

$$M[k] = |X[k]|\,. \tag{10}$$

The fault-related content was integrated over a narrow band around each expected sideband frequency. This improves robustness to spectral leakage and small frequency shifts caused by inverter-fed operation or background harmonics. For a sideband center frequency f_c, the narrowband energy was defined as

$$E(f_c) = \sum_{k:\,|f_k - f_c| \le \Delta f} M^2[k], \tag{11}$$

where $\Delta f = 2$ Hz.

For each fault type, the energies of the two expected sidebands were then summed:

$$E_{\mathrm{OR}} = E(23.64\ \mathrm{Hz}) + E(176.36\ \mathrm{Hz}), \tag{12}$$

$$E_{\mathrm{IR}} = E(23.64\ \mathrm{Hz}) + E(223.64\ \mathrm{Hz}), \tag{13}$$

$$E_{\mathrm{RE}} = E(50.08\ \mathrm{Hz}) + E(149.92\ \mathrm{Hz}). \tag{14}$$

The final indicators were defined as the corresponding narrowband amplitudes:

$$A_{\mathrm{OR}} = \sqrt{E_{\mathrm{OR}}}, \qquad A_{\mathrm{IR}} = \sqrt{E_{\mathrm{IR}}}, \qquad A_{\mathrm{RE}} = \sqrt{E_{\mathrm{RE}}}. \tag{15}$$

4.2. Bearing Fault Frequencies

The characteristic fault frequencies were calculated using the relations summarized in (Wagner & Sommer, 2021):

$$\begin{aligned} f_{\mathrm{OR}} &= \frac{N_B}{2} f_R \left(1 - \frac{D_B \cos\theta}{D_P}\right), \\ f_{\mathrm{IR}} &= \frac{N_B}{2} f_R \left(1 + \frac{D_B \cos\theta}{D_P}\right), \\ f_{\mathrm{RE}} &= \frac{D_P}{2D_B} f_R \left(1 - \frac{D_B^2 \cos^2\theta}{D_P^2}\right). \end{aligned} \tag{16}$$

where:
- N_B is the number of rolling elements,
- f_R is the shaft rotational frequency,
- D_B is the rolling element diameter,
- D_P is the pitch diameter,
- θ is the contact angle.

For the PU PMSM with $p = 4$ pole pairs, electrical fundamental is defined as:

$$f_S = p f_r. \tag{17}$$

Therefore, for the N15 condition ($f_r = 25$ Hz), the electrical frequency is around $f_S = 100$ Hz, and for N09 ($f_r = 15$ Hz) – $f_S = 60$ Hz.

For current-based analysis, the same defect frequencies are expected to appear as modulation sidebands around the electrical fundamental frequency f_S,

$$\begin{aligned} f_{\mathrm{pc,OR}} &= |f_S \pm k f_{\mathrm{OR}}|\,, \\ f_{\mathrm{pc,IR}} &= |f_S \pm k f_{\mathrm{IR}}|\,, \\ f_{\mathrm{pc,RE}} &= |f_S \pm k f_{\mathrm{RE}}|\,, \end{aligned} \tag{18}$$

where $k \in N$ denotes the sideband order. Since a one-sided magnitude spectrum was used, only non-negative frequency bins were evaluated; therefore, absolute values were used for sideband frequencies.

For the PU 6203 geometry, the first-order current sideband candidates are presented in Table 2.

Table 2. First-order current sideband candidates for the N15 operating condition.

Fault component	$f_S - f_{\mathrm{fault}}$ [Hz]	$f_S + f_{\mathrm{fault}}$ [Hz]
OR	23.64	176.36
IR	|-23.64|	223.64
RE	50.08	149.92

4.3. Indicators Evaluation

The indicators were then compared and evaluated based on 3 criteria: (i) best separability across classes, (ii) low variabil-

ity across healthy reference group, and (iii) lack of excessive correlation with operating conditions. In order to do that, the following statistics were used:

1. AUROC: measures how well the indicator separates healthy from faulty measurements; a higher value means better binary discrimination. AUROC analysis was conducted at three levels: binary separability between healthy and faulty measurements, pairwise separability between the healthy class and each fault class, and separability between the healthy class and each fault severity level.
2. healthy-vs-unhealthy absolute Cliff's delta: measures the effect size of the difference between healthy and faulty measurements; a larger absolute value means stronger separation.
3. healthy-class IQR: measures how compact and stable the indicator is within the healthy reference group; a lower value means less variability under healthy conditions.
4. Kruskal–Wallis statistic across the four class labels: measures how strongly the indicator differs across all considered classes; a higher value means better overall multiclass separability,
5. Spearman correlation coefficient ρ_s and the associated p-value: measures how much each indicator is correlated with operating conditions; lower values indicate weaker evidence of correlation.

For the separability statistics, uncertainty was estimated using a stratified recording-level bootstrap with 2000 repetitions and a fixed random seed. In each repetition, recording-level rows were resampled with replacement within the compared groups, and AUROC, absolute Cliff's delta, healthy-class IQR, and the Kruskal–Wallis statistic were recomputed. The 95% confidence intervals were obtained from the 2.5th and 97.5th percentiles of the bootstrap distributions.

5. EXPERIMENTAL SETUP

The purpose of this experiment was to identify current-derived indicators that can reflect the additional ripple introduced by bearing faults. For this reason, the analysis was initially conducted on a single operating condition and then extended to remaining ones.

- Initial Operating condition: `N15_M01_F10`, corresponding to a shaft speed of 1500 rpm, a load torque of 0.1 Nm, and a radial force of 1000 N.
- Windowing: the signal is divided into segments of length $N = 64{,}000$ samples (1 s), with an overlap of $\alpha = 0.5$ applied during train window extraction.
- Dataset size: 6 windows per measurement, 639 valid measurements originating from 32 bearings for each operating condition.

5.1. Models and Evaluation

After definition of target indicators in section 4.1.1, the five classical regressors were trained to predict the values of each indicator using only vibration data: `KNN`, `RandomForest`, `DecisionTree`, `XGBoost`, and `ElasticNet`. Their parameters were obtained through Bayesian hyperparameter search with 20 iterations and 5-fold cross-validation.

Dataset split:

- train: `K001`, `K002`, `K003`, `K004`, `K006`, `KA01`, `KA03`, `KA04`, `KA05`, `KA06`, `KA07`, `KA08`, `KA16`, `KA22`, `KA30`, `KB24`, `KB27`, `KI01`, `KI03`, `KI04`, `KI07`, `KI14`, `KI16`, `KI17`, `KI18`, `KI21`
- test: `K005`, `KA09`, `KA15`, `KB23`, `KI05`, `KI08`

All models were trained and tested on a comprehensive set of general purpose time- and frequency-domain condition indicators (Sharmaa & Parey, 2016), calculated from 64 kHz vibration channel exclusively:

- Time domain: Peak-to-peak (PP), Root Mean Square (RMS), Crest Factor (CF), Standard Deviation (STD), Kurtosis, Shape Factor (SF), EO (Energy Operator), NP4 (Normalized Peak 4th-order Statistic), FM4 (Fourth-order Figure of Merit), M6A (Sixth-order Amplitude Moment), M8A (Eighth-order Amplitude Moment), ClF (Crest Factor) II (Impulse Indicator).
- Frequency domain: Mean Frequency (MF), Frequency Center (FC), Root Mean Square Frequency (RMSF), Standard Deviation Frequency (STDF), top 3 magnitudes & their frequencies.

6. RESULTS

Figure 1 presents current RMS variability, which depends directly on torque (Figure 1a). Even though load torque was set in experiment to a constant value of 0.1 Nm, it varies from 0.59 Nm to 0.68 Nm across the whole dataset. Even across healthy bearings, current RMS values change by approximately 10% (Figure 1b), which makes it understandable that bearing faults' current losses, are not directly visible.

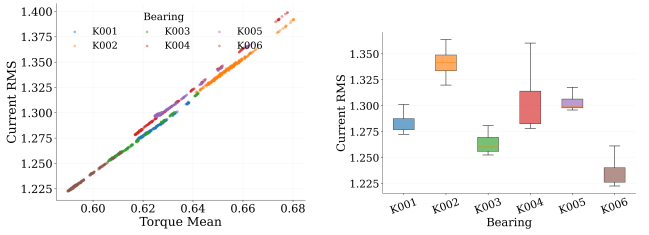

(a) variability of current RMS and torque values across dataset

(b) Current variability for healthy bearings

Figure 1. Current RMS variability across dataset.

RQ1: the PU dataset does not support a clear association between bearing faults and increased global current consump-

tion. Because each measurement lasts only 4 s and recordings were acquired across months, with changing temperature and run-in period, and with additional variations arising from the closed-loop system, a direct link between increased current and bearing faults cannot be established.

6.1. Ripple Indicators

Therefore, a natural question is which frequency bands still reveal the ripple effect caused by bearing faults and in which bands it is masked by closed-loop noise and varying operating conditions.

6.1.1. Separability and Operating-Condition Sensitivity

The main question was whether a given current-derived quantity could separate healthy bearings from faulty bearings while remaining reasonably stable. Figure 2 shows the ranking procedure for one representative operating condition, while the same procedure was repeated for all four PU operating conditions. The ranking strategy prioritized indicators that simultaneously exhibited the strongest results for evaluation methods described in 4.3.

Specifically, indicators were ranked according to: highest healthy-vs-unhealthy AUROC (Figure 2a), largest healthy-vs-unhealthy absolute Cliff's delta (Figure 2b), lowest healthy-class IQR (Figure 2c), highest Kruskal–Wallis statistic across the four class labels (Figure 2d). In Figure 2, all subplots include 95% recording-level bootstrap confidence intervals, which quantify the uncertainty of the recording-level estimates. Bold labels indicate indicators that were not statistically distinguishable from the best indicator at the defined confidence level. For 3 out of 4 rankings the best indicator was E_105_2000. For IQR, the lowest score was achieved by OR_{amp}, IR_{amp}, $G\_75\_1000\_env\_rms$, $E\_105\_2000\_env\_rms$, $B\_20\_300\_env\_rms$ and $A\_20\_150\_env\_rms$. It is clearly visible that envelope- and sideband-based indicators tend to have smaller variability across healthy condition measurements. Based on these findings, each ranking category was scored by assigning one point to all indicators that were statistically indistinguishable from the best-performing indicator. The indicators with the highest total scores were then selected as the best-performing indicators for each operating condition (Table 3).

Table 3. Best indicators for each operating condition (OC)

Operating Condition	Top indicators
N09_M07_F10	E_105_2000_env_rms, OR_amp
N15_M01_F10	E_105_2000, E_105_2000_env_rms
N15_M07_F04	E_105_2000, IRMS, IRMS_clean, IRMS_clean_env_rms, IRMS_env_rms
N15_M07_F10	E_105_2000

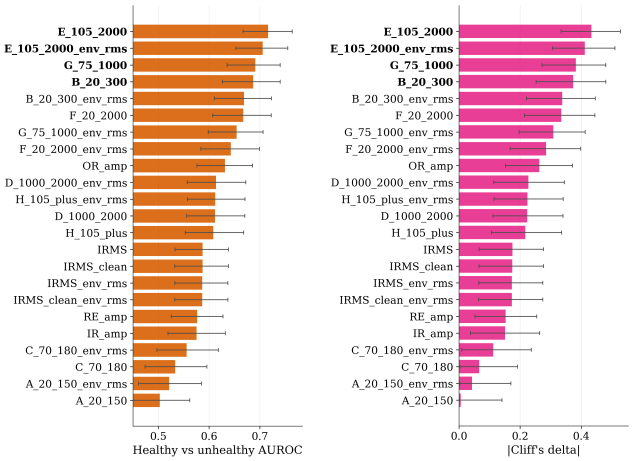

(a) healthy-vs-unhealthy AUROC (b) healthy-vs-unhealthy absolute Cliff's delta

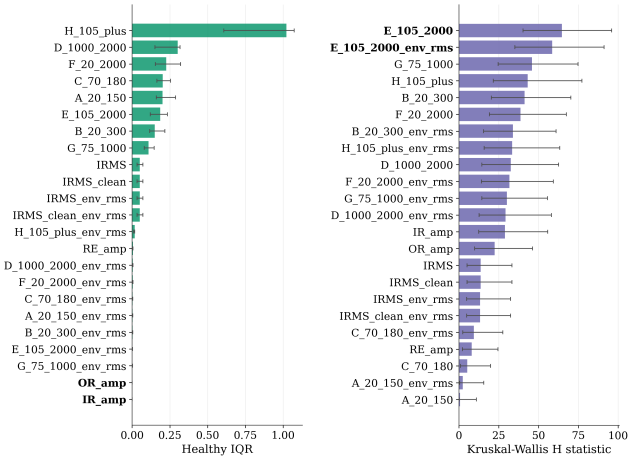

(c) healthy-class IQR (d) Kruskal–Wallis across the four class labels

Figure 2. Band and envelope indicators separability statistics for N15_M07_F04 operating conditions.

6.1.2. Separability between the healthy vs each fault class

Additionally, the AUROC statistics between healthy class and each of faulty classes was calculated (Figure 3). Here also, with bold font and asterisks, are highlighted the best indicators that are not statistically distinguishable. The best pairwise AUROC statistic for outer ring fault was achieved for E_105_2000 and $E\_105\_2000\_env\_rms$ with 0.69, comparably for B_20_300 and G_75_1000 with 0.68 and $B\_20\_300\_env\_rms$ with 0.65. Inner ring faults were best separable from healthy bearings by E_105_2000 with AUROC score 0.75, as well as by $E\_105\_2000\_env\_rms$, $D\_1000\_2000\_env\_rms$ and $H\_105\_plus\_env\_rms$. For multiple faults, the largest number of indicators achieved comparable results: IR_amp, B_20_300, G_75_1000, E_105_2000, $B\_20\_300\_env\_rms$, $E\_105\_2000\_env\_rms$, $G\_75\_1000\_env\_rms$, F_20_2000, $F\_20\_2000\_env\_rms$.

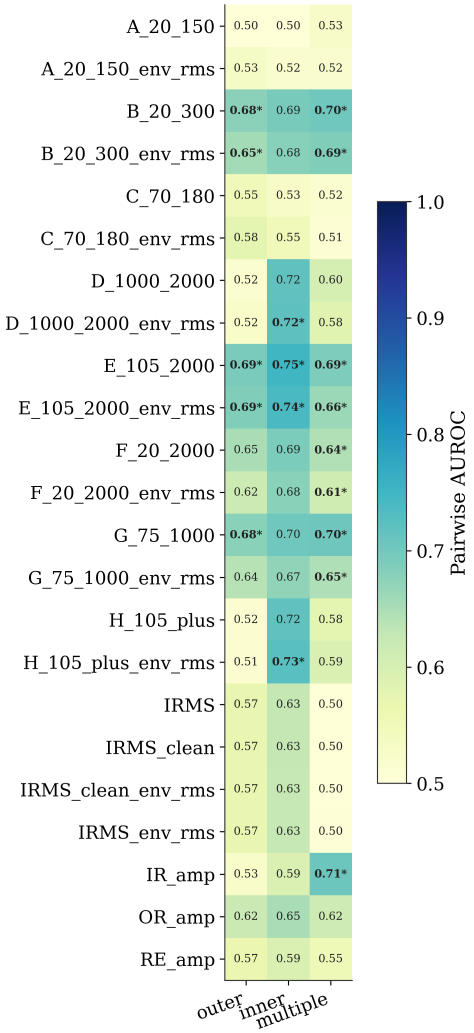

Figure 3. Pairwise AUROC heatmap healthy vs fault classes.

Table 4 summarizes the indicators that were identified as top-performing across all fault classes (healthy vs fault classes) for each operating condition. Across the four operating conditions, the most consistent results were obtained for indicators derived from the 105–2000 Hz band. E_105_2000 or its envelope-based counterpart $E\_105\_2000\_env\_rms$ appeared among the best indicators for every operating condition, indicating that this band provides the most robust fault-sensitive current information across the analyzed measurement settings.

Table 4. Top indicators across all fault classes for each operating condition.

Operating condition	Top indicators
N09_M07_F10	E_105_2000_env_rms, IRMS, IRMS_env_rms, IRMS_clean, IRMS_clean_env_rms
N15_M01_F10	E_105_2000, E_105_2000_env_rms
N15_M07_F04	E_105_2000, IRMS, IRMS_env_rms, IRMS_clean, IRMS_clean_env_rms
N15_M07_F10	E_105_2000

6.1.3. Separability between the healthy vs each severity level

Additionally, the indicators were compared with respect to fault severity level (Figure 4). In the PU dataset, faults are assigned to three severity levels, where level 1 corresponds to the lightest damage and level 3 to the strongest damage.

Table 5 summarizes the top-performing indicators for each severity level and operating condition. Indicators derived from the 105–2000 Hz band remained the most consistent for early fault signatures, since E_105_2000 or $E\_105\_2000\_env\_rms$ appeared among the best indicators for severity levels 1 and 2 in all operating conditions. For severity level 3, the best-performing indicators were more often related to global current measures or broader current-derived ripple indicators, but this pattern was less stable across operating conditions.

6.1.4. Operating conditions correlation

Finally, to quantify the remaining sensitivity of each indicator to operating-condition fluctuations, Spearman rank correlations were computed. An indicator should show strong fault separability while remaining less correlated with residual variations of speed, torque, load, and temperature within the selected nominal condition. However, it is not expected that they will be completely uncorrelated, since, as noted above, some of these mechanical signals act also as control variables in closed-loop systems (Figure 5).

Figure 6 summarizes the mean correlation values across all operating-condition signals in $-\log_{10}(p)$ scale, where clearly global RMS indicators exhibit the highest correlation to operating conditions.

Table 5. Top indicators for each fault severity level and operating condition.

Operating condition	Severity 1 and 2	Severity 3
N09_M07_F10	E_105_2000_env_rms	IR_amp_env_rms, A_20_150, A_20_150_env_rms, B_20_300
N15_M01_F10	E_105_2000, E_105_2000_env_rms	IRMS_clean_env_rms, IRMS_env_rms
N15_M07_F04	E_105_2000	IRMS, IRMS_clean, IRMS_clean_env_rms, IRMS_env_rms
N15_M07_F10	E_105_2000	D_1000_2000, D_1000_2000_env_rms, E_105_2000, E_105_2000_env_rms, G_75_1000, G_75_1000_env_rms, H_105_plus, H_105_plus_env_rms, IRMS, IRMS_clean

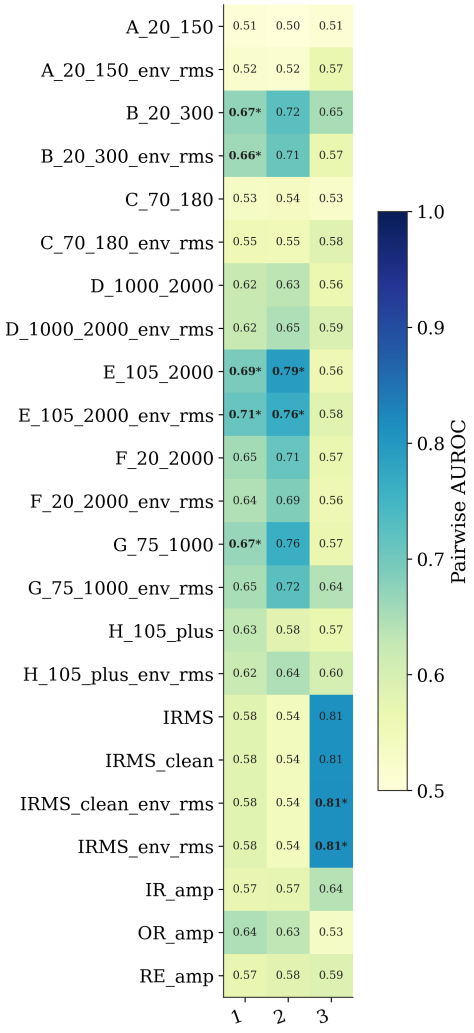

Figure 4. Pairwise AUROC heatmap for healthy measurements versus fault severity levels.

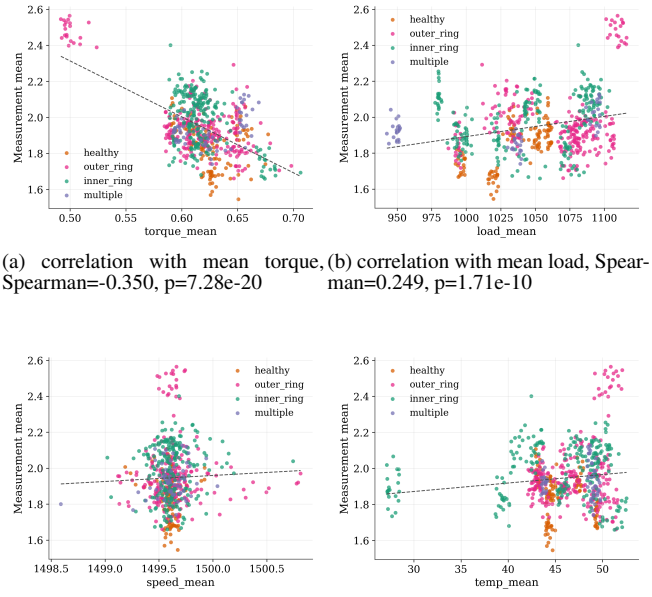

(a) correlation with mean torque, Spearman=-0.350, p=7.28e-20

(b) correlation with mean load, Spearman=0.249, p=1.71e-10

(c) correlation with mean speed, Spearman=0.050, p=2.03e-1

(d) correlation with mean temperature, Spearman=0.032, p=4.21e-01

Figure 5. Correlation plots between the best proxy E_105_2000 and operating conditions.

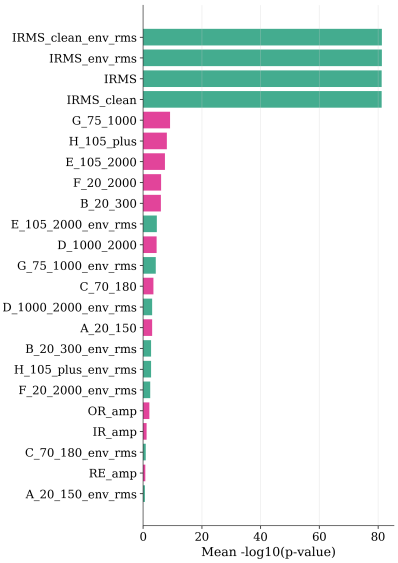

Figure 6. Mean correlation significance across operating conditions.

RQ2: the band 105–2000 Hz exhibited the strongest class separability, across operating conditions and severity levels, and moderate correlation with operating conditions, which suggests that it captures fault-related ripple more effectively than the other candidate bands while remaining reasonably robust to closed-loop control disturbances and operating-point variability.

RQ3: the band-limited current indicators were generally more informative than the classical fault-frequency sideband measures. While the sideband indicators showed competitive performance only for the multiple-fault class, the broader band indicator E_105_2000 provided the best overall separability, indicating that distributed residual ripple is a more robust fault signature than narrowly localized sideband amplitudes in this closed-loop setting.

6.2. Vibration Models

The extent to which the most informative current indicators can be explained or predicted using vibration features supports their interpretation as fault-related signals (Table 6). The strongest relationship with vibration-carried information was observed for the high-frequency indicators, especially the enveloped ones: $D\_1000\_2000\_env\_rms$ and $H\_105\_plus\_env\_rms$. Among the non-enveloped band-pass indicators, the strongest results were obtained for D_1000_2000 and E_105_2000, with R^2 values of 0.74 and 0.48, respectively.

In this study, the regression task evaluates whether a given current indicator can be reconstructed from selected vibration-derived features, which are considered the most informative diagnostic signals. Negative R^2 values were mainly observed for global current quantities such as $IRMS$, $IRMS_{clean}$. Such results may occur because current and vibration signals describe different aspects of the fault response: vibration is directly sensitive to local mechanical impacts, whereas current in a closed-loop drive reflects a more indirect electromechanical response affected by controller action, torque ripple, operating-condition changes, temperature drift, and measurement noise. In addition, the selected general vibration features may not be suitable for reconstructing specific current ripple indicators, especially with limited bearing-level diversity with a strict bearing-level resulting from a strict train-test split requiring generalization to unseen bearings. Negative R^2 may also occur when the target indicator has a small test-set variance, so even modest prediction errors become large relative to the variance to be explained. Thus, the regression results should be interpreted as evidence of vibration-based explainability rather than as a direct ranking of diagnostic usefulness. Indicators that are better reconstructed from vibration features are more likely to reflect mechanically induced fault dynamics, but their final diagnostic value should still be assessed using separability measures and dedicated classification experiments.

Although E_105_2000 was ranked as the indicator with the best class separability, its values can only be partially explained by vibration features. Figure 7 presents the indicator values predicted using vibration features only. The plots show that, for healthy bearings, both indicators take lower values than for the fault classes. However, they are still not perfectly separable from the outer-ring fault class. The highest indicator values are observed for the multiple-fault class, which is consistent with its labeling as the most severe condition (severity level 3 on a scale from 1 to 3, according to the PU dataset authors).

RQ4: the results show that several of the most informative current indicators can be at least partially explained by vibration-derived features, which supports their interpretation as manifestations of mechanically induced fault dynamics. This relationship was strongest for the higher-frequency and envelope-based indicators, particularly $D\_1000\_2000\_env\_rms$, $H\_105\_plus\_env\_rms$, and D_1000_2000.

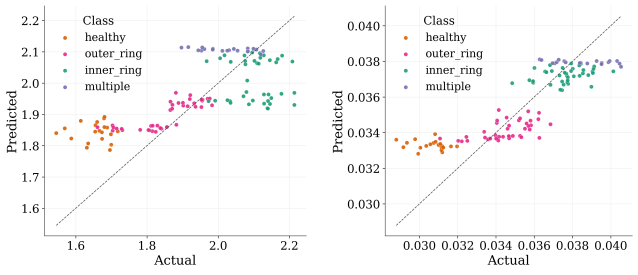

(a) E_105_2000 (b) $E\_105\_2000\_env\_rms$

Figure 7. Prediction scatter plots for E_105_2000 and $E\_105\_2000\_env\_rms$ indicators.

7. CONCLUSIONS

The main findings of this study can be summarized as follows:

- It was not possible to confirm that bearing faults lead to a clear increase in overall current consumption in a closed-loop system.
- Among the tested indicators, the band-limited RMS feature E_105_2000 provided the best overall trade-off between class separability and robustness to residual operating-condition variability.
- Broad residual-ripple bands were generally more informative than classical narrowband sideband indicators.

These findings confirm that, in closed-loop operation, RMS or total current is useful mainly for tracking the operating point, whereas the fault-related contribution remains only a small residual component.

Table 6. Best models and performance metrics sorted by descending R^2

Indicator Name	Model Name	MAE	RMSE	R^2
D_1000_2000_env_rms	KNN	0.000806	0.001116	0.853028
H_105_plus_env_rms	KNN	0.003126	0.004069	0.809326
D_1000_2000	KNN	0.064716	0.084613	0.741077
E_105_2000_env_rms	KNN	0.001302	0.001607	0.702429
E_105_2000	KNN	0.099706	0.126057	0.483280
G_75_1000_env_rms	KNN	0.001275	0.001600	0.448083
F_20_2000_env_rms	KNN	0.002479	0.003179	0.432734
H_105_plus	RF	0.392186	0.492231	0.341595
F_20_2000	KNN	0.159036	0.195087	0.335266
IR_amp	KNN	0.000236	0.000308	0.334400
OR_amp	KNN	0.000230	0.000296	0.319802
B_20_300_env_rms	KNN	0.002007	0.002573	0.186270
G_75_1000	KNN	0.096201	0.119487	0.132972
B_20_300	XGBoost	0.123900	0.157452	0.031774
RE_amp	ElasticNet	0.002620	0.002946	-0.003050
C_70_180_env_rms	RF	0.001528	0.001890	-0.017013
A_20_150_env_rms	RF	0.001975	0.002491	-0.021465
A_20_150	DT	0.111506	0.139185	-0.034237
C_70_180	DT	0.088038	0.108308	-0.053019
IRMS_env_rms	DT	0.035221	0.044028	-0.415120
IRMS_clean_env_rms	DT	0.035226	0.044034	-0.415568
IRMS	ElasticNet	0.038232	0.049042	-0.732413
IRMS_clean	ElasticNet	0.038235	0.049045	-0.732723

Therefore, the study focused on identifying the frequency bands in which fault-induced ripple remains visible while being least affected by control noise and operating-condition variability. The most useful information was found in selected ripple-oriented bands, particularly the broader post-fundamental residual bands E and D. Although a large part of the ripple energy is concentrated at low frequencies, these regions were also the most strongly affected by nuisance variability, especially bands A, B, and C located around the first harmonics and sidebands. The band-limited RMS indicators generally provided better class separability, whereas the envelope-based and higher-frequency indicators showed stronger relationships with vibration-derived fault information.

The results also show that exact narrowband sideband localization is not the most robust strategy for this dataset. Although bearing faults are classically expected to appear around the electrical fundamental and its harmonics, the proposed band-limited indicators generally provided better discrimination than the classical sideband amplitudes.

Overall, current monitoring in closed-loop systems remains promising because it relies on signals already available in the drive without the need for external components. However, its diagnostic value lies in carefully selected indicators. The proposed band-limited indicators should therefore be treated as promising monitoring and classification features that warrant further validation in dedicated classification experiments.

7.1. Limitations and Future Work

One limitation of this study is that the PU dataset reflects somewhat unstable operating conditions, primarily due to data acquisition performed across months, under varying temperatures, and with small but unavoidable variations in the measurement setup despite nominally identical configurations. Even after restricting the analysis to a single nominal operating condition, healthy measurements still exhibited substantial variability on the current RMS of approximately 10%. Consequently, for relatively small defects, tracking increased current or decreased efficiency does not appear to be sufficiently sensitive for closed-loop systems, unless the degradation is more pronounced or operating conditions are tightly controlled.

A second limitation is the interpretation of the identified ripple bands. Although several band-limited indicators showed useful fault sensitivity, the farther the analyzed band lies from the dominant electromechanical components, the less directly it can be interpreted as increased current consumption.

Finally, the diagnostic usefulness of the selected band-limited current indicators should be validated in dedicated classification experiments. Future work should therefore compare these indicators with vibration-based feature sets and investigate adaptive or order-tracked band definitions to improve robustness under varying speed and load conditions.

Acknowledgment. This work was supported by the program „Excellence Initiative – Research University" for the AGH University of Krakow.

REFERENCES

Abu-Zeid, M. A., & Abdel-Rahman, S. (2013). Bearing problems' effects on the dynamic performance of pumping stations. *Alexandria Engineering Journal*, *52*(3), 241-248.

Ackerman, K. (2023). *Life cycle costs wastewater.* Retrieved Accessed: 2025-12-12, from https://www.scribd.com/document/287097804/Life-Cycle-Costs-Wastewater (Sales Manager, Grundfos GmbH, Erkrath, Germany)

Bishop, T. H. (2024). Easa aemt study of motor repair impact on efficiency of premium efficiency (ie3) motors. In P. Radgen & P. Bertoldi (Eds.), *Energy efficiency in motor systems* (pp. 23–39). Cham: Springer Nature Switzerland.

Bravo-Imaz, I., Davari Ardakani, H., Liu, Z., García-Arribas, A., Arnaiz, A., & Lee, J. (2017). Motor current signature analysis for gearbox condition monitoring under transient speeds using wavelet analysis and dual-level time synchronous averaging. *Mechanical Systems and Signal Processing*, *94*, 73-84. doi: https://doi.org/10.1016/j.ymssp.2017.02.011

Brkovic, A., Gajic, D., Gligorijevic, J., Savic-Gajic, I., Georgieva, O., & Di Gennaro, S. (2017). Early fault detection and diagnosis in bearings for more efficient operation of rotating machinery. *Energy*, *136*, 63-71. (Renewable Energy and Energy Storage Systems)

Chen, J., Hu, W., Cao, D., Zhang, Z., Chen, Z., & Blaabjerg, F. (2023). A meta-learning method for electric machine bearing fault diagnosis under varying working conditions with limited data. *IEEE Transactions on Industrial Informatics*, *19*(3), 2552-2564. doi: 10.1109/TII.2022.3165027

Garcia, M., Panagiotou, P. A., Antonino-Daviu, J. A., & Gyftakis, K. N. (2019). Efficiency assessment of induction motors operating under different faulty conditions. *IEEE Transactions on Industrial Electronics*, *66*(10), 8072-8081.

Gritli, Y., Bellini, A., Rossi, C., Casadei, D., Filippetti, F., & Capolino, G.-A. (2017). Condition monitoring of mechanical faults in induction machines from electrical signatures: Review of different techniques. In *2017 ieee 11th international symposium on diagnostics for electrical machines, power electronics and drives (sdemped)* (p. 77-84). doi: 10.1109/DEMPED.2017.8062337

Jachymczyk, U., Knap, P., & Lalik, K. (2025). Improved intelligent condition monitoring with diagnostic indicator selection. *Sensors*, *25*(1).

Kilickaya, S., & Eren, L. (2025). Bearing fault detection in adjustable speed drives via self-organized operational neural networks. *Electrical Engineering*, *107*, 4503–4515. doi: 10.1007/s00202-024-02764-3

Korolev, N. (2025). Analytical diagnostic and control system of energy and mechanical efficiency of electric drives. *Energies*, *18*(9).

Lessmeier, C., Kimotho, J. K., Zimmer, D., & Sextro, W. (2016). Condition monitoring of bearing damage in electromechanical drive systems by using motor current signals of electric motors: A benchmark data set for data-driven classification. In *Phm society european conference* (Vol. 3). doi: 10.36001/phme.2016.v3i1.1577

Liu, Y., & Bazzi, A. M. (2017). A review and comparison of fault detection and diagnosis methods for squirrel-cage induction motors: State of the art. *ISA Transactions*, *70*, 400-409. doi: https://doi.org/10.1016/j.isatra.2017.06.001

Martin-Diaz, I., Morinigo-Sotelo, D., Duque-Perez, O., Arredondo-Delgado, P., Camarena-Martinez, D., & Romero-Troncoso, R. (2017). Analysis of various inverters feeding induction motors with incipient rotor fault using high-resolution spectral analysis. *Electric Power Systems Research*, *152*, 18-26. doi: https://doi.org/10.1016/j.epsr.2017.06.021

Randall, R. B. (2011). *Vibration-based condition monitoring: Industrial, automotive and aerospace applications*. Chichester, UK: John Wiley & Sons.

Santer, P., Reinhard, J., Schindler, A., & Graichen, K. (2025). Detection of localized bearing faults in pmsms by means of envelope analysis and wavelet packet transform using motor speed and current signals. *Mechatronics*, *106*, 103294. doi: https://doi.org/10.1016/j.mechatronics.2025.103294

Sharmaa, V., & Parey, A. (2016). A review of gear fault diagnosis using various condition indicators. *Elsevier*, *144*, 253–263.

Son, K. L. . (1982). *Monitorowanie stanu maszyn*. Denmark, Soborg: Wydawnictwo Brüel & Kjær.

Sousa Santos, V., Cabello Eras, J. J., Sagastume Gutierrez, A., & Cabello Ulloa, M. J. (2019). Assessment of the energy efficiency estimation methods on induction motors considering real-time monitoring. *Measurement*, *136*, 237-247. doi: https://doi.org/10.1016/j.measurement.2018.12.080

Wagner, T., & Sommer, S. (2021, 07). Feature based bearing fault detection with phase current sensor signals under different operating conditions. In (Vol. 6). doi: 10.36001/phme.2021.v6i1.2852

Yang, T., Pen, H., Wang, Z., & Chang, C. S. (2016). Feature knowledge based fault detection of induction motors through the analysis of stator current data. *IEEE Transactions on Instrumentation and Measurement*, *65*(3), 549-558. doi: 10.1109/TIM.2015.2498978